RSC Advances

PAPER

View Article Online
View Journal | View Issue

Check for updates

Cite this: *RSC Adv.*, 2024, **14**, 25918

Mechanisms and selectivity of methanol oxidation on $PtRuM_3$/C-MWCNT (M = Fe and Co) electrocatalysts†

Dang Long Quan,[abc] Viorel Chihaia [d] and Do Ngoc Son *[ab]

Methanol oxidation efficiency and resistance to CO poisoning are the most challenging issues associated with direct methanol fuel cells. Much experimental effort has been undertaken, such as generating Pt-based binary and ternary nanoparticles, creating composite substrates, and fabricating nanoparticles with special shapes, to overcome these drawbacks. Our previous experiment showed that ternary $PtRuM_3$/C-MWCNT (M = Fe and Co; C-MWCNT = carbon Vulcan-multiwalled carbon nanotube) electrocatalysts exhibited high methanol oxidation activity and tolerance to CO poisoning. However, reaction mechanisms on ternary $PtRuM_3$/C-MWCNT (M = Fe and Co) electrocatalysts remain unknown. Therefore, this work is devoted to elucidating the problem using density functional theory calculations and thermodynamic models. Our present study showed that methanol oxidation proceeds *via* four possible reaction pathways on the surface of $PtRuM_3$/C-MWCNTs, where the most favourable one follows a series of steps converting $CH_3OH \rightarrow CH_3OH^* \rightarrow CH_2OH^* \rightarrow CH_2O^*/CHOH^* \rightarrow CHO^* \rightarrow CHOOH^* \rightarrow CHOO^*/COOH^* \rightarrow CO_2^*$ with a thermodynamic barrier of 0.513 eV for applied potentials of U = 0 V and 1.005 V on $PtRuFe_3$/C-MWCNTs and 0.404 eV for U = 0 V and 0.167 eV for U = 1.005 V on $PtRuCo_3$/C-MWCNTs. We also provide physical insights into the interaction between methanol oxidation intermediates and substrates' surface by analysing electronic properties. Our findings support the results of our previous experiment. The results of this study can be useful for rationally designing the anode for fuel cells.

Received 19th June 2024
Accepted 3rd August 2024

DOI: 10.1039/d4ra04493b

rsc.li/rsc-advances

Open Access Article. Published on 19 August 2024. Downloaded on 7/31/2025 1:02:18 AM.
This article is licensed under a Creative Commons Attribution-NonCommercial 3.0 Unported Licence.

1 Introduction

Today, global energy shortages and environmental pollution problems have been increasing tremendously. Therefore, research on novel energy sources and technologies is an urgent requirement. Direct methanol fuel cells (DMFCs) are regarded as one of the most promising energy technologies owing to their high conversion efficiencies, low operating temperatures, and short recharge time.[1,2] Platinum is hitherto the best electrocatalyst for methanol oxidation on the anode of DMFCs because of its outstanding catalytic efficiency, excellent electrical properties, and high corrosion resistance; however, CO poisoning is the major obstacle in increasing the performance of DMFCs to a practical level.[1,2] Alloying is an effective way to enhance the activity of methanol oxidation and reduce the cost of DMFCs because of bifunctional mechanisms or electronic effects. Especially, the methanol oxidation ability of PtM (M = Fe, Co, Ni, Cu, Ru, *etc.*) binary alloys is higher than that of pure Pt,[3–10] where PtRu exhibits the highest electrocatalytic performance due to its improved tolerances to CO poisoning. From the theoretical viewpoint, adding a third metal could change PtRu electronic properties and surface structure as well as improve catalytic performance.[11,12] To date, many studies have shown that ternary Pt-based nanocrystals formed from various metals (Ru, Fe, Co, Ni, Pd, Rh, Cu, *etc.*) and support materials (carbon, carbon nanotubes, graphene, metal oxides, *etc.*) significantly enhance methanol oxidation activity and the durability of the anode of DMFCs.[13–20] Among the inexpensive metals combined with PtRu alloy, earth-abundant transition metals with low cost and good catalytic performance, such as iron (Fe), cobalt (Co), and nickel (Ni), are superior candidates for developing the anode of DMFCs.[21–30] Specifically, PtRuFe alloy displayed a higher onset potential and current intensity than PtRu and PtFe alloys.[22–24] PtRuNi alloy on Vulcan carbon and carbon nanotubes can significantly improve the methanol oxidation performance and tolerance to CO poisoning compared to PtRu alloy.[25–27] Meanwhile, PtRuCo alloy without supports also exhibited a superior ability to oxidize methanol and prevent CO poisoning compared to the PtRu alloy.[28,29] Our research recently

[a]*Ho Chi Minh City University of Technology (HCMUT), 268 Ly Thuong Kiet Street, District 10, Ho Chi Minh City, Vietnam. E-mail: dnson@hcmut.edu.vn*

[b]*Vietnam National University Ho Chi Minh City, Linh Trung Ward, Ho Chi Minh City, Vietnam*

[c]*Department of Physics, College of Natural Sciences, Can Tho University, Can Tho City, Vietnam*

[d]*Institute of Physical Chemistry "Ilie Murgulescu" of the Romanian Academy, Splaiul Independentei 202, Sector 6, 060021 Bucharest, Romania*

† Electronic supplementary information (ESI) available: Mechanisms and selectivity of methanol oxidation reaction on $PtRuM_3$/C-MWCNTs (M = Fe, Co) electrocatalysts. See DOI: https://doi.org/10.1039/d4ra04493b

© 2024 The Author(s). Published by the Royal Society of Chemistry

Open Access Article. Published on 19 August 2024. Downloaded on 7/31/2025 1:02:18 AM. This article is licensed under a Creative Commons Attribution-NonCommercial 3.0 Unported Licence.

showed that the third metal component, M, enhanced the electrocatalytic activity of $PtRuM_x$/C-MWCNTs (M = Fe, Co, Ni; x = 1, 3) compared to the binary PtRu/C-MWCNTs system. Moreover, $PtRuCo_x$/C-MWCNTs exhibited the best methanol oxidation activity, while $PtRuFe_x$/C-MWCNTs showed the highest tolerance to CO poisoning.[31]

Many theoretical studies on the interaction between methanol and catalysts have been carried out along with experiments. Using density functional theory (DFT) calculations, Zhao's group investigated the methanol oxidation on PtRu(111).[32] They found that the most favourable reaction pathway of methanol oxidation on PtRu(111) is $CH_3OH \rightarrow CH_3O \rightarrow CH_2O \rightarrow CHO \rightarrow CHOOH \rightarrow COOH \rightarrow CO_2$. Moreover, on the PtRu(111) surface, most of the intermediates adsorbed around the Ru sites due to the lower electronegativity of Ru atoms. According to Orazi *et al.*, the methanol molecule adsorbs most stably *via* its O atom on the top Co site of the PtCo(111) surface.[33] The charge transfer from the C atom to the O atom of the methanol molecule and finally to the Co atoms changed the charge distribution around the adsorption site of methanol. Du *et al.* analysed the possible mechanisms of methanol decomposition on the $Pt_3Ni(111)$ surface by examining the initial scission of O–H, C–H, and C–O bonds.[34] The DFT investigation of the reaction pathway for methanol on different Pt crystal planes and PtNi surface also suggested the Ni site as the favourable adsorption position for methanol oxidation.[35] Furthermore, the density functional studies of the CO adsorption energy on $Fe_{1-x}PtRu_x$ nanocrystal surfaces showed that the $Fe_{1-x}PtRu_x$ alloy weakens the CO–Pt bond to enhance the anti-CO poisoning ability.[36] Notably, the DFT calculations have focused only on studying the methanol oxidation on binary alloys, while there are only a few works for ternary alloy catalysts.

The experimental works confirmed that ternary PtRuM alloys without carbon supports exhibited higher methanol oxidation efficiency and CO poisoning resistance over binary Pt-based and pure metal catalysts.[22–29,31] Remarkably, our previous experiment revealed an excellent catalytic activity of $PtRuM_x$/C-MWCNTs (M = Fe, Ni, Co) and the atomic ratio of Pt : Ru : M = 1 : 1 : 3 showed a better performance than that of 1 : 1 : 1, for the methanol oxidation.[31] However, no studies are available to elucidate the methanol oxidation mechanisms of $PtRuM_x$/C-MWCNTs, particularly for Pt : Ru : M = 1 : 1 : 3. Therefore, the present work is devoted to solving this issue by systematically searching for the possible intermediates and then clarifying the reaction pathways of methanol oxidation on $PtRuM_3$/C-MWCNTs (M = Fe, Co) catalysts. Here, we selected two representatives of the electrocatalysts with M = Fe and Co because $PtRuCo_3$/C-MWCNTs showed the best reaction activity, while $PtRuFe_3$/C-MWCNTs exhibited the highest tolerance to CO poisoning among the considered third metal (Fe, Co, and Ni).[31] The results of this work are completely new and will be valuable for optimally designing ternary Pt-based catalysts. To achieve the target, we used density functional theory calculations and the thermodynamic model.[37,38]

2 Catalyst model and computational details

$PtRuFe_3$/C-MWCNTs and $PtRuCo_3$/C-MWCNTs substrates were designed using the slab model with the (111) crystal surface framework and the (4 × 4) unit cell of five atomic layers. Furthermore, to maximize the role of precious metals (Pt and Ru), we designed the supercell with the layers of these metals close to the surface of the slab. As depicted in Fig. 1a and b (top and side views), the topmost and second layers consist of sixteen Pt and sixteen Ru atoms, respectively. The underneath three layers were composed of inexpensive Fe or Co metals. The above five atomic layers are grown on the support, which consists of the graphene nanosheet with a few extra C atoms adsorbed on the bottom side of the graphene to mimic the C-MWCNTs support of the $PtRuM_3$/C-MWCNTs substrates (M = Fe and Co). The total number of atoms in each substrate is 116. We set up the substrates as described because the high-resolution transmission electron microscopy of our previous experiment exhibited that the scale of the MWCNTs is much broader than that of the nanoparticles dispersed on them. Therefore, the nanoparticle is regarded as located approximately on a nearly flat area on the surface of the MWCNT. Also, by ignoring the effects of the multiple walls, we can use a graphene sheet to mimic the MWCNT. The decorated C atoms on the bottom side of the graphene sheet mimic the Vulcan carbon in our previous experiment.[31] We expect that our supercell model can capture the main physics of the methanol oxidation on the surface of the $PtRuM_3$/C-MWCNTs catalysts. We have to emphasize that we do not intend to fully describe the MWCNTs, even though there were not many DFT calculations concerning the complexity of the model as in the present study. The *ab initio* studies have usually ignored carbon supports.[32–34,39,40] The atomic positions and the unit cell size for the designed substrates were first optimized, and the structure of possible intermediates of methanol oxidation on the optimized substrates was then fully relaxed using the density functional theory calculations with the aid of the Vienna *Ab initio* Simulation Package (VASP).[41] Our model does not include van der Waals interactions because the contribution toward chemical reactions on metal surfaces is usually ignorable.[42,43] To optimize the unit cell size, we varied the lattice constant and calculated the total energy for each variation. The minimum point in the parabolic curve of the total energy *versus* the lattice constant determines the optimized size of the unit cell, as shown in Fig. S1 in ESI.† The optimized lattice constant of both substrates is 2.61 Å. Therefore, the dimensions of the unit cell in the slab model are 10.4 Å and 10.4 Å in the x and y axes and 23.4 Å in the surface normal direction with a vacuum space of about 12 Å. In all the optimization processes for the atomic positions, the atoms were allowed to move freely in all dimensions until the force acting on each atom reached 0.001 eV $Å^{-1}$. We used a plane-wave basis set with a kinetic cut-off energy of 400 eV, the Perdew–Burke–Ernzerhof generalized gradient approximation for the exchange–correlation energy,[44,45] and the projector augmented wave pseudopotentials for the ion-valence electron interaction.[46] The k-point mesh sample of 5 × 5 × 1 with the special-point sampling

Open Access Article. Published on 19 August 2024. Downloaded on 7/31/2025 1:02:18 AM.
This article is licensed under a Creative Commons Attribution-NonCommercial 3.0 Unported Licence.

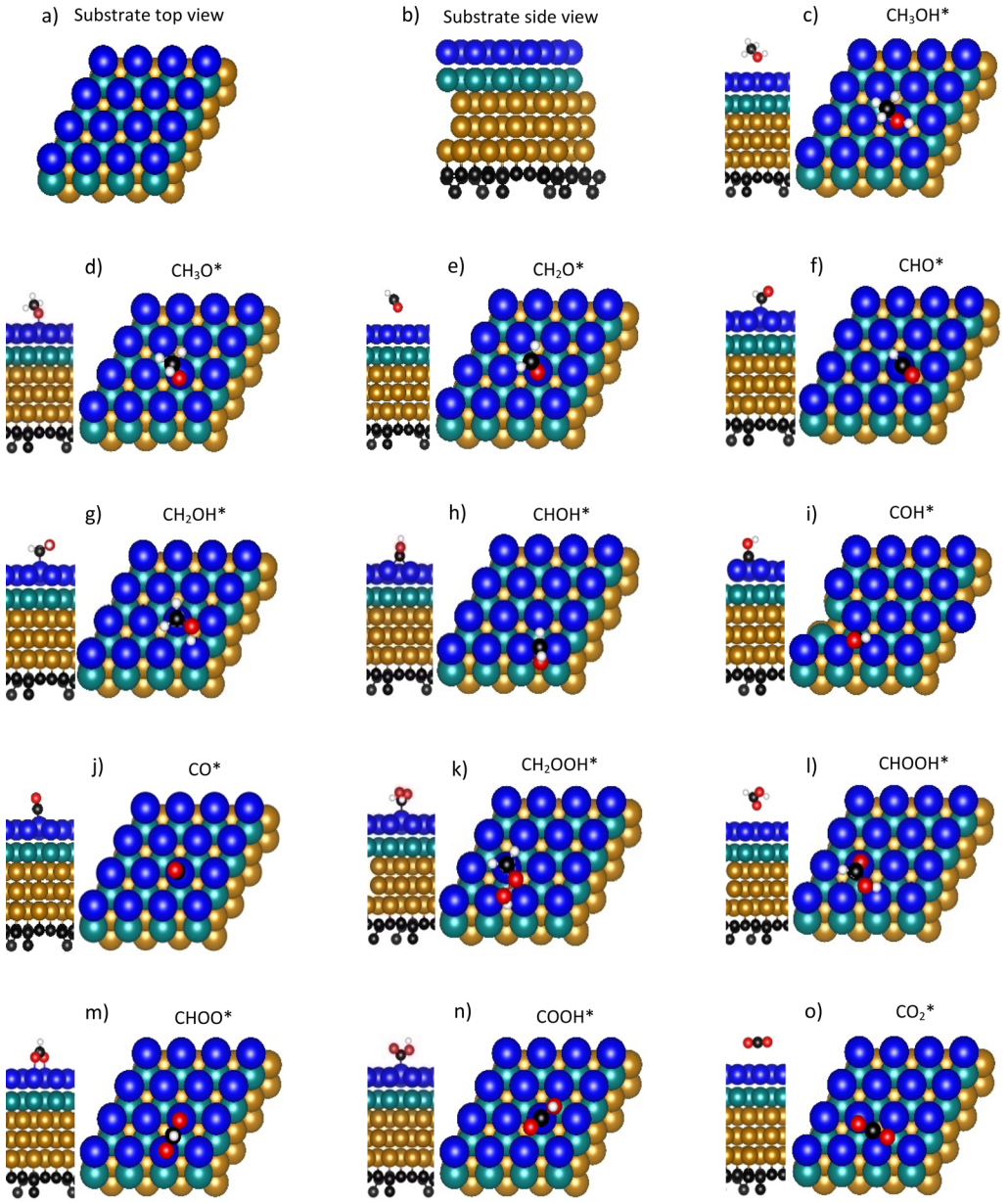

Fig. 1 The top and side views of the substrates (a and b) and the most stable configurations for the adsorption of methanol oxidation intermediates on the surface of $PtRuM_3$/C-MWCNTs (M = Fe and Co) catalysts (c–o). Topmost-layer Pt (blue), Ru (green), Fe (golden), C (black), O (red), and H (white).

technique of Monkhorst and Pack was used for the Brillouin zone integration.[47] The cut-off energy and the *k*-point mesh sample have been tested for the convergence of the total energy. Spin polarization was appropriately constructed. To simulate periodic supercells, dipole corrections were set. The convergence speed of the calculations was supported by Methfessel–Paxton smearing[48] of first order with the sigma value of 0.2 eV for geometry optimization and 0.05 eV for obtaining electronic properties.

2.1 Adsorption energy

The binding strength of the various reaction intermediates on the possible adsorption sites of the substrates is expressed *via* the adsorption energy according to the following formula:

$$E_a = E_{[sub+ads]} - (E_{sub} + E_{ads}), \quad (1)$$

where $E_{[sub+ads]}$, E_{sub}, and E_{ads} are the total energy of the substrate–adsorbate system, the clean substrate, and the isolated adsorbate, respectively. This work ignored the influences of water medium on the adsorption of the methanol oxidation intermediates.

2.2 Charge density difference

The charge density difference ($\Delta\rho$) is studied to elucidate the interaction between the adsorbent and adsorbate using the following equation:[33,38]

$$\Delta\rho = \rho_{[sub+ads]} - \rho_{sub} - \rho_{ads}, \quad (2)$$

© 2024 The Author(s). Published by the Royal Society of Chemistry

Open Access Article. Published on 19 August 2024. Downloaded on 7/31/2025 1:02:18 AM. This article is licensed under a Creative Commons Attribution-NonCommercial 3.0 Unported Licence.

where $\rho_{[sub+ads]}$, ρ_{sub}, and ρ_{ads} are the charge density of the adsorbent/adsorbate system, substrate with the adsorbed state, and the adsorbed molecule, respectively.

2.3 Gibbs free energy

Free energy diagrams following the thermodynamic model[37,49,50] were constructed to understand the thermodynamic stability of the reaction intermediates. The Gibbs free energy with electrode potential corrections was calculated as follows:

$$\Delta G(U) = \Delta G(0) + neU. \quad (3)$$

Here, $\Delta G(0) = \Delta E + \Delta ZPE - T\Delta S$ with ΔE and ΔZPE are reaction energy and the change of zero-point energies of intermediate reactions, estimated from the total energies and vibrational energies of our DFT calculations. The change in entropies (ΔS) was calculated from our DFT calculations using VASPKIT;[51] n and U are the number of electrons in each reaction step and the electrode potential relative to the standard hydrogen electrode, respectively. According to our previous experimental results,[31] the working potential of methanol oxidation was 0.8 V for the $PtRuM_3$/C-MWCNTs (M = Fe, Co) electrocatalysts relative to an Ag/AgCl (3.5 M KCl) reference electrode. Therefore, the value of U for methanol oxidation in formula (3) is equivalent to 1.005 V, *i.e.*, $E_{RHE} = E_{Ag/AgCl} + 0.205$ V, relative to the standard hydrogen electrode in our thermodynamic model. For comparison, we also studied the reaction mechanisms with $U = 0$ V. The standard atmospheric pressure of 1 bar, room temperature of 300 K, and pH = 0 were used in this study. With the pH = 0 level, we can replace the proton and electron transfer by $H^+ + e^- = \frac{1}{2}H_2$, which is adequate with the hydrogen standard electrode model.

3 Results and discussion

3.1 Adsorption configurations of intermediates

The total methanol oxidation reaction generates carbon dioxide as the following equation:

$$CH_3OH + H_2O \rightarrow CO_2 + 3H_2. \quad (4)$$

This equation can proceed in many possible pathways (see Fig. 2) with multi-intermediate steps from (1)–(18) and involve thirteen reaction intermediates. The intermediates of methanol oxidation are proposed by a continuous dehydrogenation process from the previously formed intermediates starting from CH_3OH*, where the asterisk denotes the adsorbed state of the intermediates on the substrates' surface. The dehydrogenation can take place at the hydrogen atom near the O or C atoms of each intermediate. For example, in steps (1) and (2), CH_3OH* can detach a hydrogen atom near the O atom to form CH_3O* and near the C atom to generate CH_2OH*, respectively. The other intermediates are also formed in the same manner. Noticeably, forming the double-oxygen intermediates such as CH_2OOH*, CHOOH*, and COOH* in steps (6), (11), and (16) require the involvement of a water molecule, *i.e.*, $CH_2O^* + H_2O \rightarrow CH_2OOH^* + \frac{1}{2}H_2$, $CHO^* + H_2O \rightarrow CHOOH^* + \frac{1}{2}H_2$, and $CO^* + H_2O \rightarrow COOH^*$, respectively. Here, CH_2OOH*, CHOOH*, and COOH* were formed by combining CH_2O*, CHO*, and CO* with the OH group, which stemmed from the water splitting reaction, $H_2O \rightarrow OH + \frac{1}{2}H_2$, respectively. To explore the possible intermediates of methanol oxidation reaction, we designed the structure of each intermediate on the topmost surface of the substrate with the initial position of the intermediate of about 3 Å with various directions above the surface. We then optimized all the atomic positions of the designed structure and obtained the adsorption energy. For each intermediate, we compared its adsorption energies at various adsorption sites and configurations to gauge the most favourable adsorption configuration with the most negative adsorption energy. Fig. 1c–o shows the most stable configuration for various adsorbed intermediates of the methanol oxidation reaction, *i.e.*, methanol (CH_3OH*), methoxy (CH_3O*), hydroxymethyl (CH_2OH*), formaldehyde (CH_2O*), hydroxymethylene (CHOH*), hydroperoxymethyl (CH_2OOH*), formyl (CHO*), isoformyl (COH*), formic acid (CHOOH*), carbon monoxide (CO*), formate (CHOO*), carboxyl (COOH*), and carbon dioxide (CO_2^*), on the surface of the $PtRuM_3$/C-MWCNTs (M = Fe, Co) substrates. Particularly, the adsorption site, the bond distance ($d_{ads\text{-}sur}$) from the nearest atom (carbon or oxygen atom, see Fig. 1c–o for each case) of the intermediates to the surface of the substrate, the adsorption energy (E_{ads}), the zero-point energy (ZPE), and the total energy (E_{total}, *i.e.*, E_{ads} plus ZPE) are also listed in Table 1. As shown in Fig. 1c–o, several intermediates such as CH_3OH*, CH_3O*, CH_2O*, and CHOOH* adsorb most favourably with the end-on configuration on the top (T) site of the Pt atom, where the O atom is the nearest atom to the substrates' surface. The adsorption of the other intermediates, *i.e.*, CH_2OH*, CHOH*, CH_2OOH*, CHO*, COH*, CO*, and COOH*, is also the most

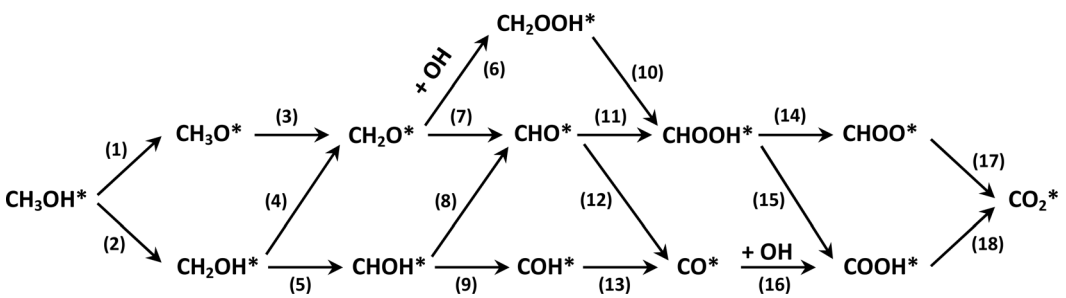

Fig. 2 Possible methanol decomposition pathways on catalyst surfaces.

Open Access Article. Published on 19 August 2024. Downloaded on 7/31/2025 1:02:18 AM. This article is licensed under a Creative Commons Attribution-NonCommercial 3.0 Unported Licence.

Table 1 The bond distance ($d_{ads\text{-}sur}$) from the nearest atom (carbon or oxygen atom) of adsorbate molecules to the surface; adsorption energy (E_{ads}), zero-point energy (ZPE), and total energy (E_{total}, *i.e.*, E_{ads} plus ZPE) of the intermediates on the $PtRuM_3$/C-MWCNT (M = Fe and Co) substrates. The top site of a Pt atom (T), the bridge of two Pt atoms (B), and the hollow with an underneath Ru atom (H)

Molecule	Chemical formula	$d_{ads\text{-}sur}$ (Å)		E_{ads} (eV)		ZPE (eV)		E_{total} (eV)	
		M = Fe (site)	M = Co (site)	M = Fe	M = Co	M = Fe	M = Co	M = Fe	M = Co
Methanol	CH_3OH^*	2.76 (T)	2.66 (T)	0.017	−0.305	1.375	1.379	1.392	1.074
Methoxy	CH_3O^*	2.17 (T)	2.15 (T)	−1.194	−1.483	1.061	1.060	−0.133	−0.423
Formaldehyde	CH_2O^*	2.97 (T)	3.07 (T)	0.072	−0.230	0.721	0.724	0.793	0.494
Formyl	CHO^*	2.36 (T)	2.37 (T)	−1.948	−2.129	0.470	0.471	−1.478	−1.658
Carbon monoxide	CO^*	2.17 (T)	2.25 (T)	−1.097	−1.335	0.203	0.205	−0.894	−1.130
Hydroxymethyl	CH_2OH^*	2.45 (T)	2.51 (T)	−1.541	−1.793	1.109	1.106	−0.432	−0.687
Hydroxymethylene	$CHOH^*$	1.88 (B)	1.94 (B)	−3.650	−3.785	0.800	0.801	−2.850	−2.984
Isoformyl	COH^*	1.47 (H)	1.47 (H)	−3.516	−3.684	0.492	0.492	−3.024	−3.192
Hydroperoxymethyl	CH_2OOH^*	2.52 (T)	2.50 (T)	−1.657	−1.835	1.162	1.171	−0.495	−0.664
Formic acid	$CHOOH^*$	2.93 (T)	3.07 (T)	0.038	−0.246	0.902	0.901	0.940	0.655
Carboxyl	$COOH^*$	2.35 (T)	2.36 (T)	−1.874	−2.139	0.616	0.616	−1.258	−1.523
Formate	$CHOO^*$	2.29 (T–T)	2.32 (T–T)	−1.947	−2.309	0.611	0.615	−1.336	−1.694
Carbon dioxide	CO_2^*	3.34 (T–B)	3.45 (T–B)	0.024	−0.206	0.316	0.316	0.340	0.110

stable with the end-on configuration *via* their C atom; however, while CH_2OH^*, CH_2OOH^*, CHO^*, COH^*, CO^*, and $COOH^*$ are on the top site, $CHOH^*$ is on the bridge (B) and COH^* is on the hollow (H) with an underneath Ru atom. Exceptions are for $CHOO^*$ and CO_2^*, where they adsorb stably in the side-on configurations with the double top (T–T) site (each O atom on a T site) for $CHOO^*$ and the T–B site (one O atom on top and the other O atom on B) for CO_2^*. Especially, the CO_2^* structure is in a straight configuration with an O–C–O angle of about 180°, parallel to the surface of the substrate. Table 1 also summarizes the most favourable adsorption site on the substrates' surface and the bond distance $d_{ads\text{-}sur}$ (in columns 3 & 4). We found that the bond distance from the nearest atom of the intermediates to the surface is in the following order: hollow < bridge < top or top–top < top-bridge. The CO_2^* intermediate is located at the largest distance of about 3.4 Å from the surface of the $PtRuM_3$/C-MWCNTs (M = Fe, Co) substrates. The adsorption energy of CH_3OH^*, CH_2O^*, $CHOOH^*$, and CO_2^* is positive (in column 5), which implies that these intermediates unfavourably adsorb and the other intermediates favourably adsorb with their negative adsorption energy on the surface of the $PtRuFe_3$/C-MWCNTs. Particularly, the adsorption energy of all the intermediates (column 6) is negative on the $PtRuCo_3$/C-MWCNTs catalyst. For each intermediate, it is more stable on $PtRuCo_3$/C-MWCNTs than on $PtRuFe_3$/C-MWCNTs because its adsorption energy is always more negative on M = Co than M = Fe in the range of about −0.135 eV ($CHOH^*$) to −0.362 eV ($CHOO^*$). The positive zero-point energy (in columns 7 & 8) competes with the negative adsorption energy and hence influences the stability of the intermediates adsorbed on the catalytic surface. We found the fluctuation (or zero-point energy) of each adsorption intermediate is rather large. Particularly, the fluctuation is stronger than the adsorption strength for CH_3OH^*, CH_2O^*, $CHOOH^*$, and CO_2^*. Therefore, the total energy E_{total} of these intermediates becomes positive, which implies that CH_3OH^*, CH_2O^*, $CHOOH^*$, and CO_2^* are unstable and subject to desorption from the substrates' surface. Emphasizing that the intermediates in the end-on *via* O configuration, such as CH_3OH^*, CH_3O^*, CH_2O^*, $CHOOH^*$, and CO_2^* in the parallel structure have positive or least negative adsorption energy, indicating the adsorption *via* the O atom is not favourable, except for $CHOO^*$. In contrast, the other intermediates remain in a stable state even after including the fluctuation on both substrates because of the negative E_{total}. The isoformyl (COH^*) is the most stable compared to all the other intermediates, with the most negative total energy on both substrates. We also found that, generally, the trend of the adsorption positions, bond distances, and adsorption energy of the intermediates are similar for both substrates, with the adsorption being more favourable on $PtRuCo_3$/C-MWCNTs than on $PtRuFe_3$/C-MWCNTs. Furthermore, the adsorption energy (E_{ads}) of formaldehyde (CH_2O^*) on $PtRuFe_3$/C-MWCNTs is insignificant, which is similar to the previous study for the adsorption of this intermediate on Pt(111).[32,52] Also, the adsorption strength of carbon monoxide (CO^*) is better on the $PtRuCo_3$/C-MWCNTs surface with an adsorption energy of −1.335 eV compared to that of −1.097 eV on the $PtRuFe_3$/C-MWCNTs surface. Interestingly, this result supports our previous experimental study, *i.e.*, the j_f/j_r ratio of peak currents in forward and reverse directions demonstrated that the resistance to CO poisoning of $PtRuFe_3$/C-MWCNTs is higher than that of $PtRuCo_3$/C-MWCNTs, with j_f/j_r values of 6.9 and 4.3, respectively.[31] The CO^* adsorption *via* the C atom on the top of the Pt atom was also found in the experiment, which investigated the CO adsorption on the Pt(111) surface by the scanning tunnelling microscopy technique.[53,54]

Furthermore, we also explored the ORR intermediates on $PtRuM_3$ substrates without C-MWCNTs support. The obtained results for the adsorption site and energy, Table S1 in ESI,† are similar to those of the $PtRuM_3$/C-MWCNTs. The most noticeable finding for the role of the C-MWCNTs support is that it enhanced the adsorption energy of the less stable intermediates

 © 2024 The Author(s). Published by the Royal Society of Chemistry

Open Access Article. Published on 19 August 2024. Downloaded on 7/31/2025 1:02:18 AM. This article is licensed under a Creative Commons Attribution-NonCommercial 3.0 Unported Licence.

like CH_3OH^*, CH_2O^*, $CHOOH^*$, and CO_2^*, where the adsorption energy of these intermediates becomes more negative on $PtRuM_3$/C-MWCNTs (Table 1) compared to the $PtRuM_3$ substrates (Table S1†), respectively.

3.2 Electronic properties

One can reveal the nature of the interaction between the intermediates and the substrates *via* the electronic structure properties such as the Bader point charge, electronic density of states, and charge density difference. The point charge is determined by the Bader partition technique[55,56] for the atoms of the substrate/intermediate systems; then, subtract the neutral charge of the atoms from the obtained point charge. Table 2 provides the Bader point charge of the C, O, and H atoms for each intermediate (columns 3–5), five atomic layers of metals (columns 6–10), and carbon layers of the substrate (column 11), where layer 1 is the topmost layer with the intermediates adsorbed on it. The total charge of each intermediate (column 12) is the charge summation of the C, H, and O atoms, while the total charge of the substrate (column 13) is calculated by the charge summation of the five atomic layers of metals and carbon layers of the substrate.

As seen in Table 2, for all the intermediates on both substrates, the C and H atoms always donate, and the O atoms always accumulate the negative charge (in the e^- unit). Also, the layer-resolved charge shows that, under the adsorption of the intermediates, layer 1 of the Pt atoms and carbon layers of both substrates always gain, and the other layers of Ru, Fe, and Co atoms always lose the charge. Although the charge accumulation and donation have such a simple rule, the total charge of the intermediate and substrate shows that the gain and loss vary for different systems. The charge exchange of CH_2O^* and $CHOOH^*$ with the substrates is ignorable because of the same magnitude, with a calculation error of $0.005e^-$. The CH_3O^*, CO^*, COH^*, $COOH^*$, and $CHOO^*$ intermediates on both substrates and CH_2OH^* on the $PtRuFe_3$/C-MWCNTs surface exhibit large charge exchanges with the substrates (more than 10% of e^- like CO^* and COH^*, to 36% of e^- as CH_3O^*, and up to 50% of e^- such as $CHOO^*$), in the magnitude order: $CHOO^* > CH_3O^* > COOH^* > COH^* > CO^* > CH_2OH^*$ for both substrates. Also, the small charge exchange (more than $0.005e^-$ and less than 10% of e^-) is found for the remaining molecules, *i.e.*, CH_3OH^*, CHO^*, $CHOH^*$, CH_2OOH^*, and CO_2^* on both substrates and CH_2OH^* on the $PtRuCo_3$/C-MWCNTs. Particularly, while CH_3OH^*, CH_2OH^*, $CHOH^*$, and CH_2OOH^* donate, the other intermediates gain the charge from the substrates. Notably, the weak charge exchange intermediates, *i.e.*, CH_3OH^*, CH_2O^*, $CHOOH^*$, and CO_2^*, have small adsorption energies, as shown in Table 1.

Table 2 The Bader charge transfer (e^-) of the substrate/intermediate systems. Positive and negative values indicate the charge gain and loss, respectively. The charge summation over all the atoms of each species in the intermediate is denoted by Σ. The error of the charge calculation is $0.005e^-$

Radical	$PtRuM_3$/C-MWCNTs	C	ΣO	ΣH	Layer 1 (Pt)	Layer 2 (Ru)	Layer 3 (Fe or Co)	Layer 4 (Fe or Co)	Layer 5 (Fe or Co)	Carbon layers	Intermediate	Substrate
CH_3OH^*	M = Fe	−0.572	1.647	−1.134	2.939	−0.519	−2.222	−0.381	−3.769	4.011	−0.059	0.059
	M = Co	−0.643	1.669	−1.066	2.929	−1.930	−0.898	−0.345	−2.619	2.903	−0.040	0.040
CH_3O^*	M = Fe	−0.692	1.159	−0.113	2.512	−0.493	−2.201	−0.373	−3.769	3.970	0.354	−0.354
	M = Co	−0.705	1.160	−0.079	2.517	−1.887	−0.906	−0.349	−2.622	2.871	0.376	−0.376
CH_2O^*	M = Fe	−1.580	1.734	−0.155	2.909	−0.545	−2.217	−0.384	−3.768	4.006	−0.001	0.001
	M = Co	−1.632	1.756	−0.121	2.883	−1.929	−0.895	−0.344	−2.620	2.902	0.003	−0.003
CHO^*	M = Fe	−1.671	1.793	−0.112	2.793	−0.387	−2.217	−0.396	−3.767	3.964	0.010	−0.010
	M = Co	−1.583	1.799	−0.138	2.731	−1.790	−0.907	−0.349	−2.621	2.858	0.078	−0.078
CO^*	M = Fe	−1.760	1.880	—	2.665	−0.394	−2.216	−0.368	−3.768	3.961	0.120	−0.120
	M = Co	−1.736	1.870	—	2.688	−1.825	−0.906	−0.334	−2.621	2.864	0.134	−0.134
CH_2OH^*	M = Fe	−0.773	1.810	−1.156	2.910	−0.403	−2.218	−0.391	−3.765	3.986	−0.119	0.119
	M = Co	−0.729	1.811	−1.127	2.839	−1.804	−0.902	−0.347	−2.620	2.879	−0.045	0.045
$CHOH^*$	M = Fe	−0.862	1.915	−1.112	2.776	−0.308	−2.225	−0.391	−3.766	3.973	−0.059	0.059
	M = Co	−0.846	1.937	−1.125	2.780	−1.733	−0.917	−0.345	−2.621	2.870	−0.034	0.034
COH^*	M = Fe	−0.921	2.042	−1.000	2.529	−0.250	−2.234	−0.395	−3.768	3.997	0.121	−0.121
	M = Co	−0.865	2.045	−1.000	2.512	−1.685	−0.937	−0.337	−2.623	2.890	0.180	−0.180
CH_2OOH^*	M = Fe	−0.741	1.850	−1.183	2.876	−0.392	−2.217	−0.386	−3.766	3.959	−0.074	0.074
	M = Co	−0.625	1.840	−1.234	2.833	−1.794	−0.909	−0.346	−2.620	2.855	−0.019	0.019
$CHOOH^*$	M = Fe	−2.723	3.802	−1.084	2.924	−0.547	−2.219	−0.380	−3.767	3.994	−0.005	0.005
	M = Co	−2.675	3.768	−1.089	2.898	−1.939	−0.891	−0.341	−2.621	2.890	0.004	−0.004
$COOH^*$	M = Fe	−2.691	3.870	−1.000	2.619	−0.407	−2.222	−0.377	−3.767	3.975	0.179	−0.179
	M = Co	−2.643	3.860	−1.000	2.599	−1.821	−0.902	−0.345	−2.620	2.872	0.217	−0.217
$CHOO^*$	M = Fe	−2.783	3.366	−0.093	2.412	−0.542	−2.201	−0.362	−3.768	3.971	0.490	−0.490
	M = Co	−2.742	3.369	−0.128	2.401	−1.906	−0.909	−0.337	−2.620	2.872	0.499	−0.499
CO_2^*	M = Fe	−4.000	4.024	—	2.922	−0.543	−2.220	−0.379	−3.767	3.963	0.024	−0.024
	M = Co	−4.000	4.030	—	2.891	−1.925	−0.896	−0.342	−2.622	2.864	0.030	−0.030

Open Access Article. Published on 19 August 2024. Downloaded on 7/31/2025 1:02:18 AM.
This article is licensed under a Creative Commons Attribution-NonCommercial 3.0 Unported Licence.

From the above analysis, we can state that the interaction between the methanol oxidation reaction intermediates and the substrates is the charge exchange; except for CH_2O* and CHOOH*, the interaction should be due to the charge attraction (no charge exchange).

The subtle physical insights into the interaction of the intermediates and the substrates are also revealed *via* analysing the electronic density of states (DOS). We first present the orbital-projected DOS of the isolated intermediates to identify the location of peaks (Fig. 3) before considering their interaction with the substrates. We then show the orbital-projected DOS of the adsorbed intermediates to determine at which peaks the modification occurs the most to understand the changes in the DOS due to the substrate–adsorbate interaction (Fig. 4).

Fig. 3 shows that all the isolated intermediates have a peak near or at the Fermi level, which can be the spin-up or spin-down components or both. The p_x orbital dominates this peak for the double O intermediates such as CH_2OOH, CHOOH, CHOO, COOH, and CO_2. For the other intermediates, the dominated orbital can be the p_y orbital for CH_3OH, CH_2OH, CHOH, CH_2O, and CHO, and the p_z orbital for CH_3O, COH, and CO. The s orbital contributes to the peak at the Fermi level for most of the intermediates, except for CO and CO_2. However, this contribution is much smaller than the p orbitals.

The orbital-projected electronic density of states of the substrate/intermediate systems in Fig. 4 and S2, ESI,† will assist in substantially understanding the nature of the interaction between the intermediates and the substrates. In Fig. 4 and S2,† we plotted only the most significant orbitals near the Fermi level, in the energy range from −4.0 to 2.0 eV. We presented the identical orbitals with the same colour, *i.e.*, d_{xz} and d_{yz} (green) and d_{xy} and $d_{x^2-y^2}$ (black). We found that the spin-up d_{xz}, d_{yz}, and d_{z^2} orbitals of the Pt, Ru, Co, and Fe metal atoms and all the spin-down d orbitals (*i.e.*, d_{xy}, $d_{x^2-y^2}$, d_{xz}, d_{yz}, d_{z^2}) of the metal atoms dominate the DOS of the $PtRuCo_3$/C-MWCNTs and $PtRuFe_3$/C-MWCNTs substrates around the Fermi level. Notably, the orbitals of the carbon support are insignificant. The interaction between an adsorbate and an adsorbent is established by the attraction between the occupied states of the adsorbate and the unoccupied states of the adsorbent and *vice versa*. Comparing the orbital-projected DOS of the adsorbed intermediates in Fig. 4 and S2† to that of the isolated intermediates in Fig. 3, we found that the peak at the Fermi level of the isolated intermediates disappears in the adsorbed intermediates (Fig. 4) and rearranges clearly inside the valence and conduction bands. Tracking the DOS of the isolated intermediates at the Fermi level, we can conclude that the interaction between the p orbitals, *i.e.*, (p_x, p_y, p_z) of all the intermediates with the *z*-axis projected spin-up d orbitals and all the spin-down d orbitals of the Pt, Ru, Co, and Fe atoms is the physical reason for the adsorption of the intermediates on the $PtRuM_3$/C-MWCNTs substrates.

Fig. 5 depicts the charge density difference of the substrate/intermediate systems, where the cyan and yellow colours present the charge depletion and accumulation, respectively.

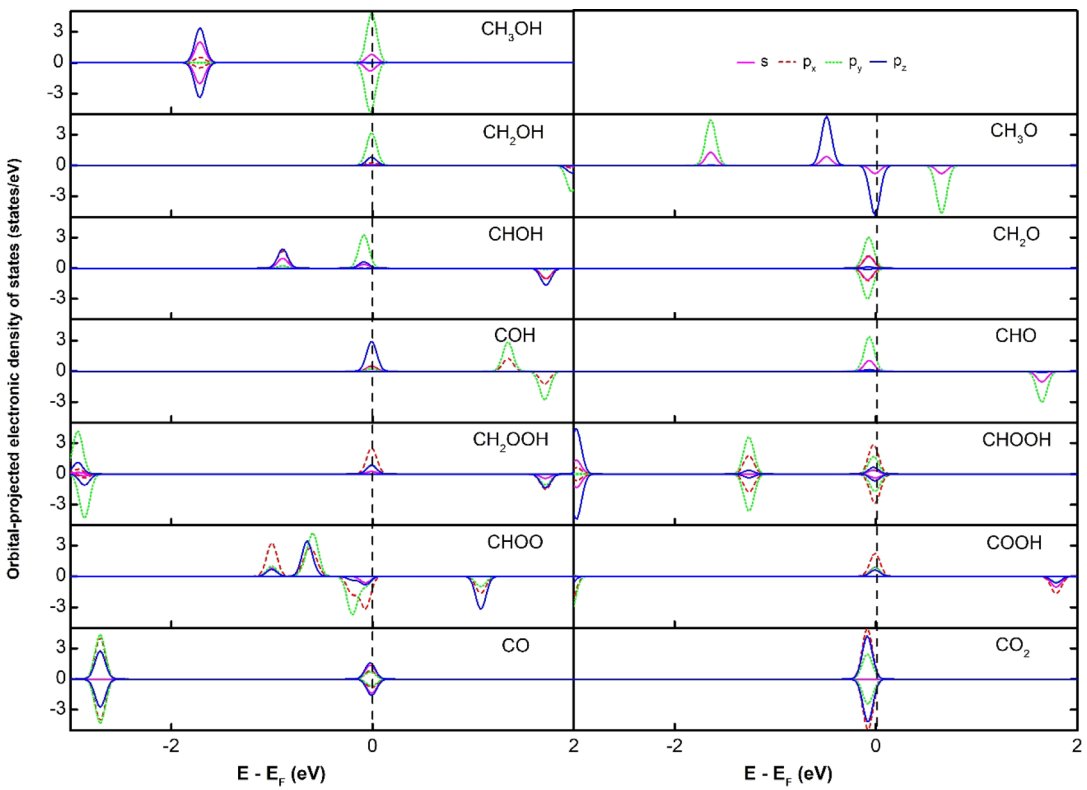

Fig. 3 The orbital-projected electronic density of states of the isolated adsorbates.

© 2024 The Author(s). Published by the Royal Society of Chemistry

Open Access Article. Published on 19 August 2024. Downloaded on 7/31/2025 1:02:18 AM.
This article is licensed under a Creative Commons Attribution-NonCommercial 3.0 Unported Licence.

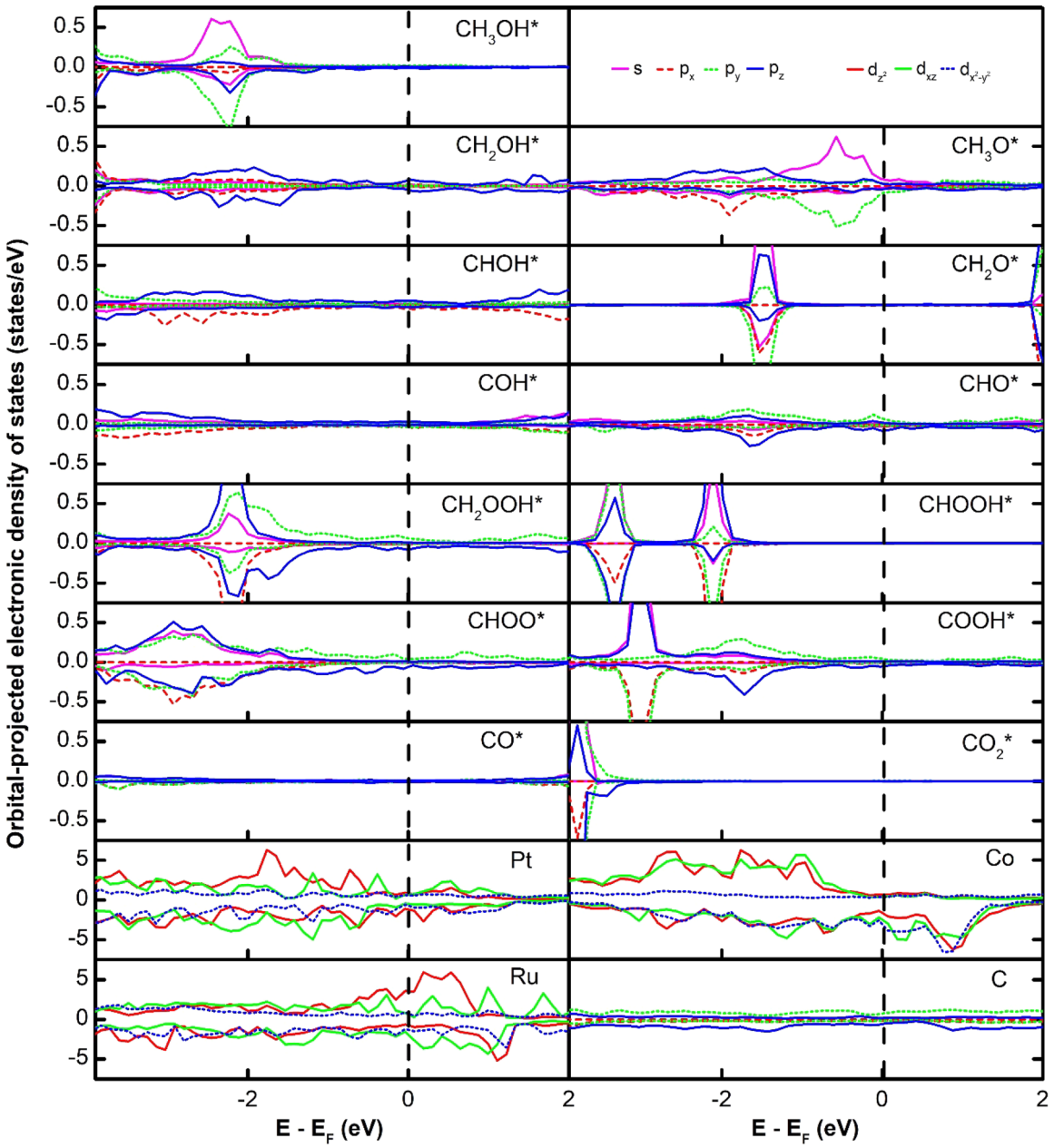

Fig. 4 The orbital-projected electronic density of states for the systems of the $PtRuCo_3$/C-MWCNT substrate and the adsorbed intermediate: d_{xz} is identical to d_{yz}, and d_{xy} is identical to $d_{x^2-y^2}$. For the $PtRuFe_3$/C-MWCNT substrate, see Fig. S2 in ESI.†

We found that the topmost Pt layer (layer 1 in Table 2) and the O atom of the intermediates always gain charge. Therefore, if the CH_3OH*, CH_3O*, CH_2O*, CHOOH*, CO_2^*, and CHOO* intermediates approach the substrate surface, their O atom will compete with the Pt layer to gain the charge. Therefore, the interface region between the O atom and the surface will form the depletion cloud (cyan colour). This cyan cloud couples with the accumulation clouds to form charge dipoles while it simultaneously couples with the charge gain cloud of the O atom of the intermediates to form another charge dipole. Therefore, the intermediates and the substrates can establish the interaction *via* these dipoles. If the depletion cloud in the interface region is broad, the intermediates such as CH_3OH*, CH_3O*, CH_2O*, CHOOH*, and CO_2^* compete strongly with the Pt layer. Hence, their interaction with the substrate surface becomes weak, resulting in unstable adsorption, as analysed in Subsection 3.1. Although CHOO* also adsorbs *via* the O atoms, its charge dipoles are arranged more harmonically and equitably. The other strongly adsorbed intermediates also have characteristics similar to those of the charge arrangement of CHOO*.

Crystal orbital Hamilton population (COHP) can also provide a better understanding of the chemical bonding strength of the intermediates to the substrate surface.[57–59] Fig. 6 shows the

Open Access Article. Published on 19 August 2024. Downloaded on 7/31/2025 1:02:18 AM.
This article is licensed under a Creative Commons Attribution-NonCommercial 3.0 Unported Licence.

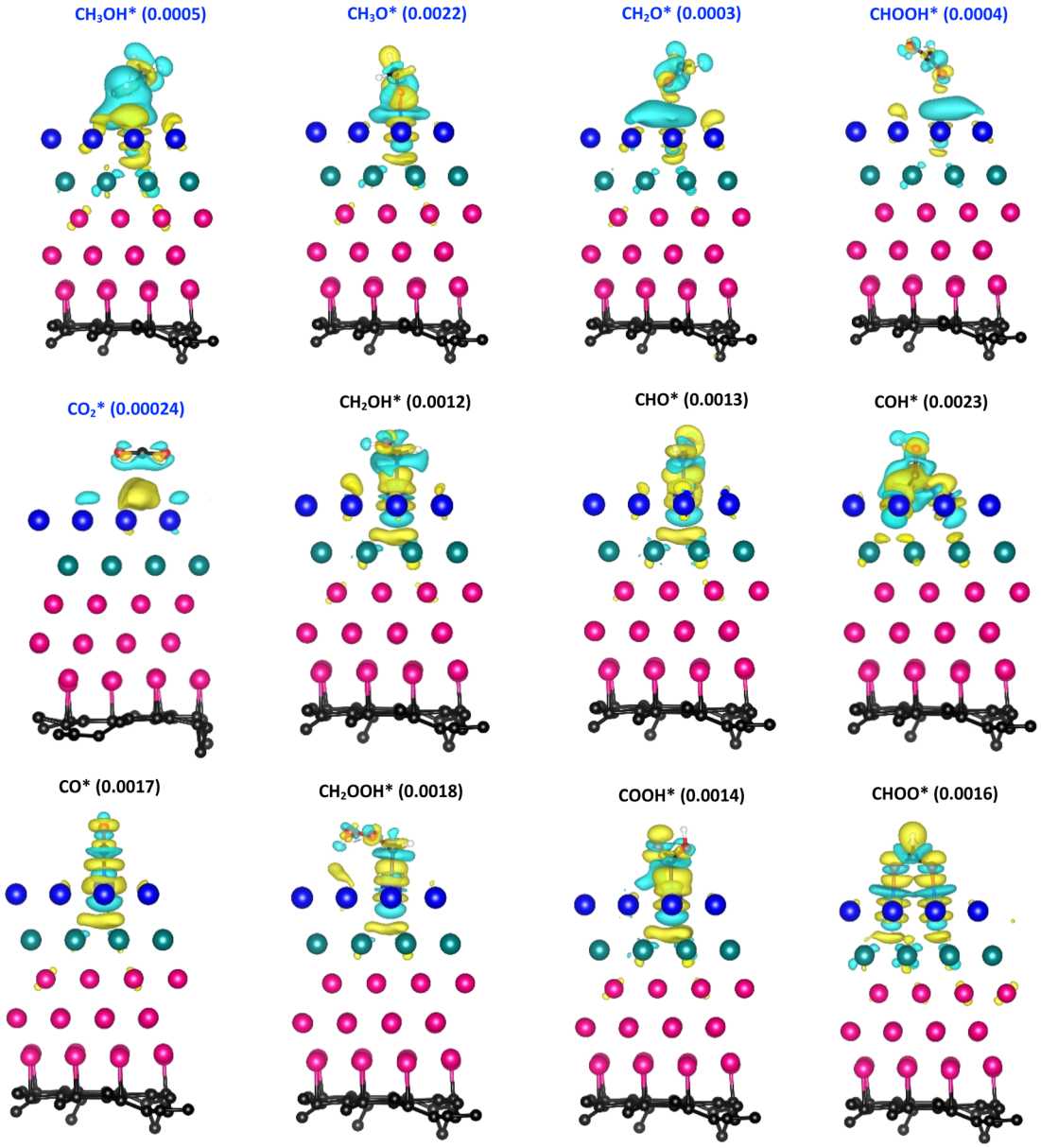

Fig. 5 The charge density difference of the systems of the adsorbed intermediate on the $PtRuCo_3$/C-MWCNT substrate. The isosurface values are inside parentheses, with the unit being e^- Å^{-3}.

COHP, the O–Pt bond, between the oxygen atoms of the representative intermediates (CH_3OH*, CH_3O*, and CH_2O*) and the $PtRuCo_3$/C-MWCNTs substrate. The positive and negative values of the COHP describe the binding and antibonding energy regions, respectively. The results implied that the O–Pt interaction is the strongest for CH_3O* and weakest for CH_3OH* and CH_2O*, which agrees well with the trend of their adsorption energies and the Bader charge transfers.

3.3 Methanol oxidation reaction mechanisms

Fig. 2 presents the possible reaction pathways on the surface of the $PtRuM_3$/C-MWCNTs substrates, which are expressed in detail through the following intermediate reactions:

$$CH_3OH^* + H_2O \rightleftarrows CH_3O^* + \tfrac{1}{2}H_2 + H_2O, \quad (R1)$$

$$CH_3OH^* + H_2O \rightleftarrows CH_2OH^* + \tfrac{1}{2}H_2 + H_2O, \quad (R2)$$

$$CH_3O^* + \tfrac{1}{2}H_2 + H_2O \rightleftarrows CH_2O^* + H_2 + H_2O, \quad (R3)$$

$$CH_2OH^* + \tfrac{1}{2}H_2 + H_2O \rightleftarrows CH_2O^* + H_2 + H_2O, \quad (R4)$$

$$CH_2OH^* + \tfrac{1}{2}H_2 + H_2O \rightleftarrows CHOH^* + H_2 + H_2O, \quad (R5)$$

$$CH_2O^* + H_2 + H_2O \rightleftarrows CH_2OOH^* + 3/2H_2, \quad (R6)$$

$$CH_2O^* + H_2 + H_2O \rightleftarrows CHO^* + 3/2H_2 + H_2O, \quad (R7)$$

$$CHOH^* + H_2 + H_2O \rightleftarrows CHO^* + 3/2H_2 + H_2O, \quad (R8)$$

© 2024 The Author(s). Published by the Royal Society of Chemistry

Open Access Article. Published on 19 August 2024. Downloaded on 7/31/2025 1:02:18 AM.
This article is licensed under a Creative Commons Attribution-NonCommercial 3.0 Unported Licence.

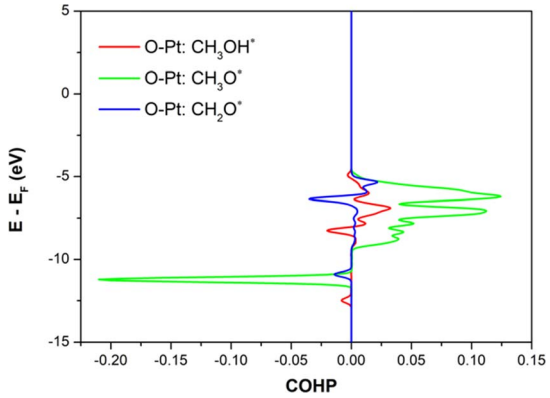

Fig. 6 The crystal orbital Hamilton population of the O–Pt bonding interaction between the intermediates (CH_3OH*, CH_3O*, and CH_2O*) and the $PtRuCo_3$/C-MWCNT substrate.

$$CHOH^* + H_2 + H_2O \rightleftarrows COH^* + 3/2H_2 + H_2O, \quad (R9)$$

$$CH_2OOH^* + 3/2H_2 \rightleftarrows CHOOH^* + 2H_2, \quad (R10)$$

$$CHO^* + 3/2H_2 + H_2O \rightleftarrows CHOOH^* + 2H_2, \quad (R11)$$

$$CHO^* + 3/2H_2 + H_2O \rightleftarrows CO^* + 2H_2 + H_2O, \quad (R12)$$

$$COH^* + 3/2H_2 + H_2O \rightleftarrows CO^* + 2H_2 + H_2O, \quad (R13)$$

$$CHOOH^* + 2H_2 \rightleftarrows CHOO^* + 5/2H_2, \quad (R14)$$

$$CHOOH^* + 2H_2 \rightleftarrows COOH^* + 5/2H_2, \quad (R15)$$

$$CO^* + 2H_2 + H_2O \rightleftarrows COOH^* + 5/2H_2, \quad (R16)$$

$$CHOO^* + 5/2H_2 \rightleftarrows CO_2^* + 3H_2, \quad (R17)$$

$$COOH^* + 5/2H_2 \rightleftarrows CO_2^* + 3H_2. \quad (R18)$$

The formula to calculate the Gibbs free energy for each intermediate step from (R1)–(R18) is presented as follows[60]

$$\Delta G_i(U) = G_{iR}(U) - G_{iL}(U) = \Delta G_i(0) + eU, \quad (5)$$

$$\Delta G_i(0) = G_{iR}(0) - G_{iL}(0). \quad (6)$$

where i runs from (R1)–(R18). L and R denote the left and right sides of each intermediate step, from (R1)–(R18). G_i and ΔG_i indicate the Gibbs free energy for one side of the reaction and the whole intermediate step, respectively.

To identify the favourable reaction pathways, we calculated the Gibbs free energy (ΔG)[61] for all intermediate steps from (R1)–(R18) with zero-point energies provided in Table 1. To do that, we first have to attain the values of the Gibbs free energy G_{iL} and G_{iR} as listed in Table 3 for the applied potential $U = 0$ V. We then calculate $\Delta G_i(0)$, following eqn (6), for the applied potential $U = 0$ V, and determine $\Delta G_i(U)$, following eqn (5), for $U = 1.005$ V. Fig. 7 and 8 depict the Gibbs free energy diagrams for methanol oxidation reaction on the $PtRuFe_3$/C-MWCNTs and $PtRuCo_3$/C-MWCNTs substrates at the applied potentials $U =$ 0 and 1.005 V, respectively.

We first analyse the reaction mechanisms of methanol oxidation on the $PtRuFe_3$/C-MWCNTs substrate at the applied potential $U = 0$ V, see Fig. 7a and Table 4. Note that we did not study transition states for the intermediate steps in the present work. In the forward direction, Fig. 7 shows the possible pathways: path 1 converts $CH_3OH \rightarrow CH_3OH^* \rightarrow CH_2OH^* \rightarrow CH_2O^*/CHOH^* \rightarrow CHO^* \rightarrow CHOOH^* \rightarrow CHOO^*/COOH^* \rightarrow CO_2^*$ going uphill from $CH_3OH \rightarrow CH_3OH^* \rightarrow CH_2OH^* \rightarrow CH_2O^*$ and $CHO^* \rightarrow CHOOH^* \rightarrow CHOO^*$, where the rate-limiting step occurs at the methanol adsorption step ($CH_3OH \rightarrow CH_3OH^*$) with the thermodynamic barrier of 0.513 eV (see Table 4). Path 2 transforms $CH_3OH \rightarrow CH_3OH^* \rightarrow CH_2OH^* \rightarrow CH_2O^*/CHOH^* \rightarrow CHO^*/COH^* \rightarrow CO^* \rightarrow COOH^* \rightarrow CO_2^*$, which goes uphill from $CH_3OH \rightarrow CH_3OH^* \rightarrow CH_2OH^* \rightarrow CH_2O^*/CHOH^*$ and $CO^* \rightarrow COOH^*$, where the rate-limiting step happens at the carbon monoxide to carboxyl converting step ($CO^* \rightarrow COOH^*$) with the thermodynamic barrier of 0.786 eV on $PtRuFe_3$/C-MWCNTs (see Table 4). Path 3: $CH_3OH \rightarrow CH_3OH^* \rightarrow CH_3O^* \rightarrow CH_2O^* \rightarrow CHO^*$

Table 3 The Gibbs free energy G_{iL} and G_{iR} (eV) of the intermediate steps on the $PtRuM_3$/C-MWCNTs (M = Fe and Co) substrates at an applied potential (U) of 0 V, pressure of 1 bar, and temperature of 300 K

Intermediate step	$PtRuFe_3$/C-MWCNTs	$PtRuCo_3$/C-MWCNTs
$CH_3OH^* + H_2O$	0.513	0.167
$CH_3O^* + 1/2H_2 + H_2O$	1.357	1.037
$CH_2OH^* + 1/2H_2 + H_2O$	0.653	0.388
$CH_2O^* + H_2 + H_2O$	1.084	0.792
$CHOH^* + H_2 + H_2O$	1.127	0.641
$CHO^* + 3/2H_2 + H_2O$	0.508	0.398
$COH^* + 3/2H_2 + H_2O$	0.879	0.716
$CH_2OOH^* + 3/2H_2$	3.696	3.503
$CO^* + 2H_2 + H_2O$	0.003	−0.260
$CHOOH^* + 2H_2$	0.835	0.548
$CHOO^* + 5/2H_2$	0.997	0.634
$COOH^* + 5/2H_2$	0.789	0.453
$CO_2^* + 3H_2$	0.329	0.033

Open Access Article. Published on 19 August 2024. Downloaded on 7/31/2025 1:02:18 AM.
This article is licensed under a Creative Commons Attribution-NonCommercial 3.0 Unported Licence.

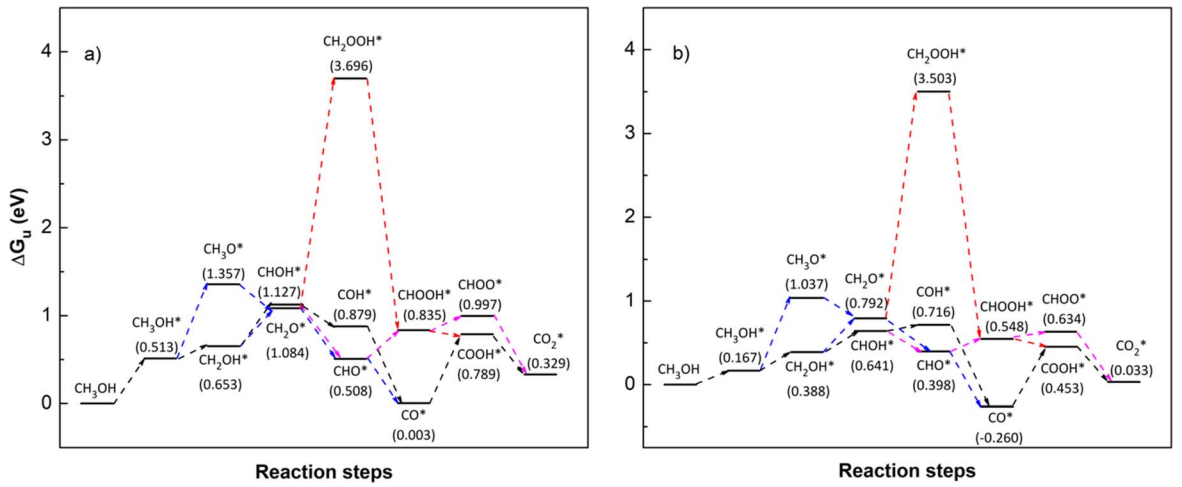

Fig. 7 Gibbs free energy diagram for the methanol oxidation reaction on (a) $PtRuFe_3$/C-MWCNT and (b) $PtRuCo_3$/C-MWCNT substrates at an applied potential (U) of 0 V, a pressure of 1 bar, and a temperature of 300 K. For simplicity, the hydrogen and water molecules in each step have been omitted in the diagrams. Relative Gibbs free energy (eV) is in parenthesis.

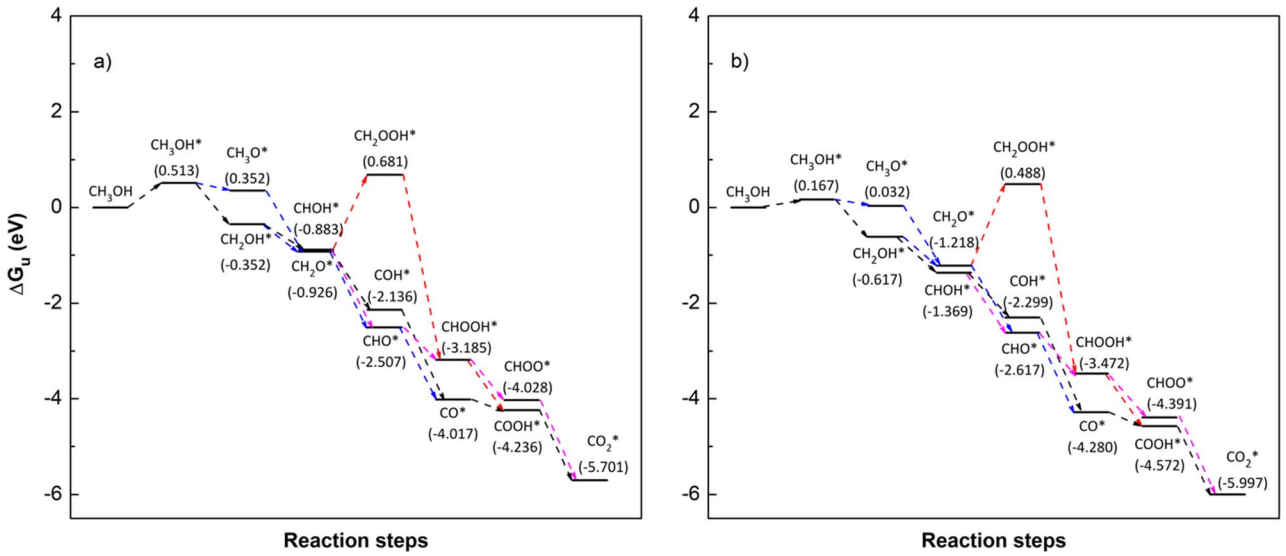

Fig. 8 Gibbs free energy diagram for the methanol oxidation reaction on (a) $PtRuFe_3$/C-MWCNT and (b) $PtRuCo_3$/C-MWCNT substrates at an applied potential (U) of 1.005 V, pressure of 1 bar, and temperature of 300 K. For simplicity, the hydrogen and water molecules in the reaction equations have been omitted in the diagrams. Relative Gibbs free energy (eV) is in parenthesis.

$\rightarrow CHOOH^*/CO^* \rightarrow CHOO^*/COOH^* \rightarrow CO_2^*$ with the rate-limiting step taking place at the methanol to methoxy transforming step ($CH_3OH^* \rightarrow CH_3O^*$) with a thermodynamic barrier of 0.844 eV (Table 4). Path 4: $CH_3OH \rightarrow CH_3OH^* \rightarrow CH_3O^*/CH_2OH^* \rightarrow CH_2O^* \rightarrow CH_2OOH^* \rightarrow CHOOH^* \rightarrow CHOO^*/COOH^* \rightarrow CO_2^*$ with the rate-limiting step occurs at the formaldehyde to hydroperoxymethyl converting step ($CH_2O^* \rightarrow CH_2OOH^*$) with a thermodynamic barrier of 2.612 eV. We can see that the four reaction pathways are found not only on the $PtRuFe_3$/C-MWCNTs but also on the $PtRuCo_3$/C-MWCNTs substrate. However, the rate-limiting step of path 1 occurs at the hydroxymethyl to formaldehyde transforming step ($CH_2OH^* \rightarrow CH_2O^*$) on the $PtRuCo_3$/C-MWCNTs substrate, which is different from that on the $PtRuFe_3$/C-MWCNTs surface. The highest thermodynamic barrier (E_b) for path 1, path 2, path 3, and path 4 on the $PtRuCo_3$/C-MWCNTs substrate is 0.404, 0.713, 0.870, and 2.711 eV, respectively. According to the Arrhenius equation for calculating the reaction-rate constant (R), $R \sim \exp(-E_b/RT)$, the lower the barrier, the higher the favourable order of the reaction pathway should be. We found that the favourable order of reaction pathways is path 1 > path 2 > path 3 > path 4 for both substrates. By comparing the energy barrier for each path, we found that path 1 and path 2 of the methanol oxidation reaction are more favourable on $PtRuCo_3$/C-MWCNTs than on $PtRuFe_3$/C-MWCNTs, while path 3 and path 4 are slightly less favourable on $PtRuCo_3$/C-MWCNTs. Notably, path 4 has a very high thermodynamic barrier, which perhaps

© 2024 The Author(s). Published by the Royal Society of Chemistry

Open Access Article. Published on 19 August 2024. Downloaded on 7/31/2025 1:02:18 AM. This article is licensed under a Creative Commons Attribution-NonCommercial 3.0 Unported Licence.

Table 4 The thermodynamic barrier (eV) of the intermediate steps on the $PtRuM_3$/C-MWCNTs (M = Fe, Co) substrates at the applied potential U = 0 V, pressure of 1 bar, and temperature of 300 K. The rate-limiting step is marked by bold font. The highest thermodynamic barrier for each pathway is presented in parentheses

Intermediate step	$PtRuFe_3$/C-MWCNTs	$PtRuCo_3$/C-MWCNTs
$CH_3OH + H_2O \rightarrow CH_3OH^* + H_2O$	**0.513 (path 1)**	0.167
$CH_3OH^* + H_2O \rightarrow CH_3O^* + 1/2H_2 + H_2O$	**0.844 (path 3)**	**0.870 (path 3)**
$CH_3OH^* + H_2O \rightarrow CH_2OH^* + 1/2H_2 + H_2O$	0.140	0.221
$CH_3O^* + 1/2H_2 + H_2O \rightarrow CH_2O^* + H_2 + H_2O$	−0.273	−0.245
$CH_2OH^* + 1/2H_2 + H_2O \rightarrow CH_2O^* + H_2 + H_2O$	0.431	**0.404 (path 1)**
$CH_2OH^* + 1/2H_2 + H_2O \rightarrow CHOH^* + H_2 + H_2O$	0.474	0.253
$CH_2O^* + H_2 + H_2O \rightarrow CH_2OOH^* + 3/2H_2$	**2.612 (path 4)**	**2.711 (path 4)**
$CH_2O^* + H_2 + H_2O \rightarrow CHO^* + 3/2H_2 + H_2O$	−0.576	−0.394
$CHOH^* + H_2 + H_2O \rightarrow CHO^* + 3/2H_2 + H_2O$	−0.619	−0.243
$CHOH^* + H_2 + H_2O \rightarrow COH^* + 3/2H_2 + H_2O$	−0.248	0.075
$CH_2OOH^* + 3/2H_2 \rightarrow CHOOH^* + 2H_2$	−2.861	−2.955
$CHO^* + 3/2H_2 + H_2O \rightarrow CHOOH^* + 2H_2$	0.327	0.150
$CHO^* + 3/2H_2 + H_2O \rightarrow CO^* + 2H_2 + H_2O$	−0.505	−0.658
$COH^* + 3/2H_2 + H_2O \rightarrow CO^* + 2H_2 + H_2O$	−0.876	−0.976
$CHOOH^* + 2H_2 \rightarrow CHOO^* + 5/2H_2$	0.162	0.086
$CHOOH^* + 2H_2 \rightarrow COOH^* + 5/2H_2$	−0.046	−0.095
$CO^* + 2H_2 + H_2O \rightarrow COOH^* + 5/2H_2$	**0.786 (path 2)**	**0.713 (path 2)**
$CHOO^* + 5/2H_2 \rightarrow CO_2^* + 3H_2$	−0.668	−0.601
$COOH^* + 5/2H_2 \rightarrow CO_2^* + 3H_2$	−0.460	−0.420

prohibits the methanol oxidation reaction from proceeding on both substrates.

From the above analysis, our results exhibited that, for U = 0 V, path 1 is the most favourable mechanism: $CH_3OH \rightarrow CH_3OH^* \rightarrow CH_2OH^* \rightarrow CH_2O^*/CHOH^* \rightarrow CHO^* \rightarrow CHOOH^* \rightarrow CHOO^*/COOH^* \rightarrow CO_2$ on both substrates. Compared to the literature, our result is different from the work of Lv *et al.*,[35] where they found that the most favourable mechanism for the methanol oxidation on Pt and PtNi catalysts should proceed *via* the CO* formation, *i.e.*, $CH_3OH^* \rightarrow CH_2OH^* \rightarrow CHOH^* \rightarrow COH^* \rightarrow CO^* \rightarrow COOH^* \rightarrow CO_2^*$. Besides, the most favourable pathway on PtRu/Pt(111) in the research of Ding *et al.*,[42] is $CH_3OH^* \rightarrow CH_3O^* \rightarrow CH_2O^* \rightarrow CHO^* \rightarrow HCOOH^* \rightarrow COOH^* \rightarrow CO_2^*$, where forming CH_3O^* does not result in the most favourable mechanism for the $PtRuCo_3$/C-MWCNTs and $PtRuFe_3$/C-MWCNTs substrates in our present work. The most favourable reaction pathway (path 1) in this study supports the previous experiments that $PtRuCo_3$/C-MWCNTs and $PtRuFe_3$/C-MWCNTs catalysts have higher tolerances to CO poisoning compared to the Pt-based bimetallic alloys.[31,62]

At the experimental condition, U = 1.005 V relative to the hydrogen standard electrode, Fig. 8 shows that all of path 1, path 2, and path 3 are going downhill after the uphill step at $CH_3OH \rightarrow CH_3OH^*$. Therefore, all three pathways have the same rate-limiting step at $CH_3OH \rightarrow CH_3OH^*$ and the same thermodynamic barrier of 0.513 eV and 0.167 eV on both $PtRuCo_3$/C-MWCNTs and $PtRuFe_3$/C-MWCNTs substrates, respectively. The barrier on $PtRuCo_3$/C-MWCNTs is three times lower than that on $PtRuFe_3$/C-MWCNTs, implying that the third metal component Co offers a significantly better performance over Fe. Interestingly, this result is consistent with our experiment,[31] where $PtRuCo_3$/C-MWCNTs showed a considerably higher methanol oxidation peak and significantly lower electron transfer resistance compared to $PtRuFe_3$/C-MWCNTs. Besides, path 4 has the rate-limiting step occurring at the converting step from formaldehyde to hydroperoxymethyl ($CH_2O^* \rightarrow CH_2OOH^*$), which is the same as that at the applied potential U = 0 V; however, the activation barrier of 1.607 and 1.705 eV on the $PtRuCo_3$/C-MWCNTs and $PtRuFe_3$/C-MWCNTs surfaces, respectively. Also, the activation barrier for path 4 at U = 1.005 V is significantly lower than that at U = 0 V.

We also calculated the Gibbs free energy and studied Gibbs free energy diagrams at the applied potentials of U = 0 V and 1.005 V for the methanol oxidation reaction on $PtRuM_3$ catalysts without the C-MWCNTs support. The Gibbs free energy diagrams are also similar to those on the $PtRuM_3$/C-MWCNTs; however, the activation barrier differs. Comparing Tables 4 and S2† shows that, in the presence of the C-MWCNTs support, this value at U = 0 V increases for path 1, path 2 and decreases for path 3, path 4 on $PtRuM_3$/C-MWCNTs (M = Fe and Co). At U = 1.005 V, the energy barrier for the three most favourable pathways (path 1, path 2, and path 3; three paths have the same energy barrier for each metal M = Fe and Co) on $PtRuM_3$ substrates is 0.417 eV (Fe) and 0.376 eV (Co), and that for the most unfavourable one (*via* CH_2OOH^*) is 1.732 eV (Fe) and 1.953 eV (Co). We found that the C-MWCNTs support increases the activation barrier for the three most favourable paths on $PtRuFe_3$/C-MWCNTs, while it decreases for all the other cases. Therefore, the C-MWCNTs support plays a better role for the $PtRuCo_3$/C-MWCNTs.

4 Conclusions

Using density functional theory calculations, we searched for the possible intermediates of methanol oxidation reaction on

Open Access Article. Published on 19 August 2024. Downloaded on 7/31/2025 1:02:18 AM. This article is licensed under a Creative Commons Attribution-NonCommercial 3.0 Unported Licence.

the surface of $PtRuM_3$/C-MWCNTs (M = Fe and Co) substrates. Most intermediates stably adsorb except for methanol, formaldehyde, formic acid, and carbon dioxide. The interaction between the intermediates and the substrates is due to the charge exchange for all intermediates, excluding the electrostatic attraction with CH_2O and CHOOH, which mainly stems from the p orbitals of the intermediates interacting with the *z*-axis projected spin-up components of and all the spin-down component of the d orbitals of the Pt, Ru, Co, and Fe atoms. The Gibbs free energy diagram showed four possible reaction pathways for the methanol oxidation on the $PtRuM_3$/C-MWCNTs (M = Fe and Co) substrates. At the applied potential of 0 V, three most favourable mechanisms with different activation barriers on each substrate are (path 1) $CH_3OH \rightarrow CH_3OH^* \rightarrow CH_2OH^*$ $\rightarrow CH_2O^*/CHOH^* \rightarrow CHO^* \rightarrow CHOOH^*$ $\rightarrow CHOO^*/COOH^* \rightarrow CO_2^*$, (path 2) $CH_3OH \rightarrow CH_3OH^* \rightarrow CH_2OH^*$ $\rightarrow CH_2O^*/CHOH^* \rightarrow CHO^*/COH^* \rightarrow CO^* \rightarrow COOH^* \rightarrow CO_2^*$, and (path 3) $CH_3OH \rightarrow CH_3OH^* \rightarrow CH_2OH^*$ $\rightarrow CH_2O^*/CHOH^* \rightarrow CHO^*/COH^* \rightarrow CO^* \rightarrow COOH^* \rightarrow CO_2^*$, However, at the working potential of 1.005 V, these pathways have the same downhill behaviour, with the highest thermodynamic barrier occurring at the methanol adsorption step, $CH_3OH \rightarrow CH_3OH^*$. Three pathways have the same energy barrier of 0.513 and 0.167 eV for the $PtRuFe_3$/C-MWCNTs and $PtRuCo_3$/C-MWCNTs substrates, respectively. This result implied that the performance of $PtRuCo_3$/C-MWCNTs is better than that of $PtRuFe_3$/C-MWCNTs. This study only considered the low coverage of reaction intermediates. However, further investigation of the effects of coverages is necessary for understanding a full physical picture of the interaction between the intermediates and the substrate surface, which will be a research topic for future studies.

Data availability

The data supporting this article have been included as part of the ESI.†

Author contributions

Conceptualization (DNS), formal analysis (DNS, DLQ), investigation (DLQ, DNS), resources (DNS, VC), supervision (DNS, VC), validation (DNS, DLQ, VC), visualization (DLQ), writing manuscript (DNS, DLQ), reviewing and editing (DNS, VC).

Conflicts of interest

There are no conflicts of interest to declare.

Acknowledgements

This research is funded by Vietnam National University Ho Chi Minh City (VNU-HCM) under grant number VL2022-20-01.

References

1 A. Yuda, A. Ashok and A. Kumar, *Catal. Rev.*, 2022, **64**, 126–228.
2 Q. Lu, X. Zhao, R. Luque and K. Eid, *Coord. Chem. Rev.*, 2023, **493**, 215280.
3 J. Xu, K. Hua, G. Sun, C. Wang, X. Lv and Y. Wang, *Electrochem. Commun.*, 2006, **8**, 982–986.
4 R. Baronia, J. Goel, S. Tiwari, P. Singh, D. Singh, S. P. Singh and S. K. Singhal, *Int. J. Hydrogen Energy*, 2017, **42**, 10238–10247.
5 A. B. A. A. Nassr, I. Sinev, W. Grünert and M. Bron, *Appl. Catal., B*, 2013, **142**, 849–860.
6 J. Sun, Y. Hou, X. Wang, T. Kou, N. Liu, R. Zhang and Z. Zhang, *RSC Adv.*, 2021, **11**, 14970–14979.
7 J. Maya-Cornejo, A. Garcia-Bernabé and V. Compañ, *Int. J. Hydrogen Energy*, 2018, **43**, 872–884.
8 S. Das and P. P. Kundu, *RSC Adv.*, 2015, **5**, 93539–93546.
9 Q. Lu, J. Huang, C. Han, L. Sun and X. Yang, *Electrochim. Acta*, 2018, **266**, 305–311.
10 H. Zhao, W. Qi, X. Zhou, H. Wu and Y. Li, *Chin. J. Catal.*, 2018, **39**, 342–349.
11 V. Stamenkovic, B. S. Mun, K. J. J. Mayrhofer, P. N. Ross, N. M. Markovic, J. Rossmeisl, J. Greeley and J. K. Nørskov, *Angew. Chem.*, 2006, **45**, 2897–2901.
12 P. Strasser, Q. Fan, M. Devenney, W. H. Weinberg, P. Liu and J. K. Nørskov, *J. Phys. Chem. B*, 2003, **107**, 11013–11021.
13 M. E. Scofield, C. Koenigsmann, L. Wang, H. Liu and S. S. Wong, *Energy Environ. Sci.*, 2015, **8**, 350–363.
14 Q. Zhao, G. Zhang, G. Xu, Y. Li, B. Liu, X. Gong, D. Zheng, J. Zhang and Q. Wang, *Appl. Surf. Sci.*, 2016, **389**, 181–189.
15 Y. Yang, L. M. Luo, R. H. Zhang, J. J. Du, P. C. Shen, Z. X. Dai, C. Sun and X. W. Zhou, *Electrochim. Acta*, 2016, **222**, 1094–1102.
16 C. Shang, Y. Guo and E. Wang, *Nano Res.*, 2018, **11**, 4348–4355.
17 K. Deng, Y. Xu, C. Li, Z. Wang, H. Xue, X. Li, L. Wang and H. Wang, *Langmuir*, 2018, **35**, 413–419.
18 H. Wang, Y. Wu, X. Luo, L. Jiao, X. Wei, W. Gu, D. Du, Y. Lin and C. Zhu, *Nanoscale*, 2019, **11**, 10575–10580.
19 Y. Pan, H. Li, Z. Wang, Y. Han, Z. Wu, X. Zhang, J. Lai, L. Wang and S. Feng, *Chem. Commun.*, 2020, **56**, 9028–9031.
20 W. Zhao, F. Xie, M. Gan, L. Ma, Y. Zhang, X. Li, L. Wang and X. Hua, *Mater. Today Chem.*, 2022, **24**, 100788.
21 X. Ren, Q. Lv, L. Liu, B. Liu, Y. Wang, A. Liu and G. Wu, *Sustainable Energy Fuels*, 2020, **4**, 15–30.
22 M. K. Jeon, J. Y. Won, K. R. Lee and S. I. Woo, *Electrochem. Commun.*, 2007, **9**, 2163–2166.
23 M. K. Jeon, K. R. Lee, H. Daimon, A. Nakahara and S. I. Woo, *Catal. Today*, 2008, **132**, 123–126.
24 Z. Cai, Y. Kuang, X. Qi, P. Wang, Y. Zhang, Z. Zhang and X. Sun, *J. Mater. Chem. A*, 2015, **3**, 1182–1187.
25 Z. B. Wang, G. P. Yin, Y. Y. Shao, B. Q. Yang, P. F. Shi and P. X. Feng, *J. Power Sources*, 2007, **165**, 9–15.
26 Y. Zhao, L. Fan, J. Ren and B. Hong, *Int. J. Hydrogen Energy*, 2014, **39**, 4544–4557.

© 2024 The Author(s). Published by the Royal Society of Chemistry

Open Access Article. Published on 19 August 2024. Downloaded on 7/31/2025 1:02:18 AM. This article is licensed under a Creative Commons Attribution-NonCommercial 3.0 Unported Licence.

27 H. Lee, S. Park and H. Kim, *Chem. Eng. J.*, 2021, **414**, 128792.
28 T. Huang, J. Liu, R. Li, W. Cai and A. Yu, *Electrochem. Commun.*, 2009, **11**, 643–646.
29 T. Huang, X. Wang, J. Zhuang, W. B. Cai and A. Yu, *Electrochem. Solid-State Lett.*, 2009, **12**, B112–B115.
30 M. Semasko, L. Tamasauskaite-Tamasiunaite, V. Kepeniene, A. Balciunaite, J. Vaiciuniene, A. Drabavicius and E. Norkus, *ECS Trans.*, 2015, **68**, 55–62.
31 D. L. Quan, P. T. Hai, P. H. Le and D. N. Son, *Res. Chem. Intermed.*, 2023, **49**, 3987–4007.
32 L. Zhao, S. Wang, Q. Ding, W. Xu, P. Sang, Y. Chi, X. Lu and W. Guo, *J. Phys. Chem. C*, 2015, **119**, 20389–20400.
33 V. Orazi, P. Bechthold, P. V. Jasen, R. Faccio, M. E. Pronsato and E. A. Gonzalez, *Appl. Surf. Sci.*, 2017, **420**, 383–389.
34 P. Du, P. Wu and C. Cai, *J. Phys. Chem. C*, 2017, **121**, 9348–9360.
35 Q. Lv, X. Ren, L. Liu, W. Guan and A. Liu, *Ionics*, 2020, **26**, 1325–1336.
36 D. Y. Wang, H. L. Chou, Y. C. Lin, F. J. Lai, C. H. Chen, J. F. Lee, B. J. Hwang and C. C. Chen, *J. Am. Chem. Soc.*, 2012, **134**, 10011–10020.
37 J. K. Nørskov, J. Rossmeisl, A. Logadottir, L. Lindqvist, J. R. Kitchin, T. Bligaard and H. Jónsson, *J. Phys. Chem. B*, 2004, **108**, 17886–17892.
38 H. T. Thanh, O. K. Le, V. Chihaia and D. N. Son, *Phys. Chem. Chem. Phys.*, 2024, **26**, 3963–3973.
39 D. N. Son, H. Nakanishi, M. Y. David and H. Kasai, *J. Phys. Soc. Jpn.*, 2009, **78**, 114601.
40 D. N. Son, P. N. Thanh, N. D. Quang, K. Takahashi and M. P. Pham-Ho, *J. Appl. Electrochem.*, 2017, **47**, 747–754.
41 G. Kresse and J. Furthmuller, *Phys. Rev. B: Condens. Matter Mater. Phys.*, 1996, **54**, 11169–11186.
42 Q. Ding, W. Xu, P. Sang, J. Xu, L. Zhao, X. He and W. Guo, *Appl. Surf. Sci.*, 2016, **369**, 257–266.
43 F. Chiter, V. B. Nguyen, N. Tarrat, M. Benoit, H. Tang and C. Lacaze-Dufaure, *Mater. Res. Express*, 2016, **3**, 046501.
44 J. P. Perdew, J. A. Chevary, S. H. Vosko, K. A. Jackson, M. R. Pederson, D. J. Singh and C. Fiolhais, *Phys. Rev. B: Condens. Matter Mater. Phys.*, 1992, **46**, 6671–6687.
45 J. P. Perdew, K. Burke and M. Ernzerhof, *Phys. Rev. Lett.*, 1996, **77**, 3865–3868.
46 G. Kresse and D. Joubert, *Phys. Rev. B: Condens. Matter Mater. Phys.*, 1999, **59**, 1758–1775.
47 H. J. Monkhorst and J. D. Pack, *Phys. Rev. B: Solid State*, 1976, **13**, 5188–5192.
48 M. Methfessel and A. T. Paxton, *Phys. Rev. B: Condens. Matter Mater. Phys.*, 1989, **40**, 3616–3621.
49 D. N. Son and K. Takahashi, *J. Phys. Chem. C*, 2012, **116**, 6200–6207.
50 D. N. Son, O. K. Le, V. Chihaia and K. Takahashi, *J. Phys. Chem. C*, 2015, **119**, 24364–24372.
51 V. Wang, N. Xu, J. C. Liu, G. Tang and W. T. Geng, *Comput. Phys. Commun.*, 2021, **267**, 108033.
52 J. Greeley and M. Mavrikakis, *J. Am. Chem. Soc.*, 2004, **126**, 3910–3919.
53 J. A. Stroscio and D. M. Eigler, *Science*, 1991, **254**, 1319–1326.
54 M. Ø. Pedersen, M. L. Bocquet, P. Sautet, E. Lægsgaard, I. Stensgaard and F. Besenbacher, *Chem. Phys. Lett.*, 1999, **299**, 403–409.
55 G. Henkelman, A. Arnaldsson and H. Jonsson, *Comput. Mater. Sci.*, 2006, **36**, 354–360.
56 D. N. Son, T. T. T. Huong and V. Chihaia, *RSC Adv.*, 2018, **8**, 38648–38655.
57 S. Xia and S. Bobev, *J. Alloys Compd.*, 2007, **427**, 67–72.
58 X. Li and F. Peng, *Phys. Chem. Chem. Phys.*, 2019, **21**, 15609–15614.
59 A. V. Kovalenko, A. V. Bandura, D. D. Kuruch, S. I. Lukyanov and R. A. Evarestov, *Phys. Status Solidi B*, 2021, **258**, 2100072.
60 O. M. Na, N. T. X. Huynh, P. T. Thi, V. Chihaia and D. N. Son, *RSC Adv.*, 2020, **10**, 8460–8469.
61 T. P. Dung, V. Chihaia and D. N. Son, *RSC Adv.*, 2023, **13**, 8523–8534.
62 H. Li, Y. Pan, D. Zhang, Y. Han, Z. Wang, Y. Qin, S. Lin, X. Wu, H. Zhao, J. Lai, B. Huang and L. Wang, *J. Mater. Chem. A*, 2020, **8**, 2323–2330.

© 2024 The Author(s). Published by the Royal Society of Chemistry